Journal of Geophysical Research: Oceans

RESEARCH ARTICLE
10.1029/2018JC014381

Wave Generation, Dissipation, and Disequilibrium in an Embayment With Complex Bathymetry

Jia-Lin Chen[1], **David K. Ralston**[2], **W. Rockwell Geyer**[2], **Christopher K. Sommerfield**[3], **and Robert J. Chant**[4]

[1]Department of Hydraulic and Ocean Engineering, National Cheng Kung University, Tainan, Taiwan, [2]Woods Hole Oceanographic Institution, Woods Hole, MA, USA, [3]College of Earth, Ocean, & Environment, University of Delaware, Lewes, DE, USA, [4]Department of Marine and Coastal Sciences, State University of New Jersey, Rutgers, New Brunswick, NJ, USA

Key Points:
- Steeply sloping bathymetry forces significant departures in wave height from equilibrium with local water depth
- Despite relatively shallow depth, whitecapping dominates wave dissipation, with bottom friction also significant over steep, linear ridges
- Bathymetric change due to dredging has had minimal impact on wave climate because waves in the channel remain far from equilibrium

Correspondence to:
J.-L. Chen,
jialinchenpsu@gmail.com

Citation:
Chen, J.-L., Ralston, D. K., Geyer, W. R., Sommerfield, C. K., & Chant, R. J. (2018). Wave generation, dissipation, and disequilibrium in an embayment with complex bathymetry. *Journal of Geophysical Research: Oceans*, *123*, 7856–7876. https://doi.org/10.1029/2018JC014381

Received 25 JUL 2018
Accepted 30 SEP 2018
Accepted article online 4 OCT 2018
Published online 6 NOV 2018

Abstract Heterogeneous, sharply varying bathymetry is common in estuaries and embayments, and complex interactions between the bathymetry and wave processes fundamentally alter the distribution of wave energy. The mechanisms that control the generation and dissipation of wind waves in an embayment with heterogeneous, sharply varying bathymetry are evaluated with an observational and numerical study of the Delaware Estuary. Waves in the lower bay depend on both local wind forcing and remote wave forcing from offshore, but elsewhere in the estuary waves are controlled by the local winds and the response of the wavefield to bathymetric variability. Differences in the wavefield with wind direction highlight the impacts of heterogeneous bathymetry and limited fetch. Under the typical winter northwest wind conditions waves are fetch-limited in the middle estuary and reach equilibrium with local water depth only in the lower bay. During southerly wind conditions typical of storms, wave energy is near equilibrium in the lower bay, and midestuary waves are attenuated by the combination of whitecapping and bottom friction, particularly over the steep, longitudinal shoals. Although the energy dissipation due to bottom friction is generally small relative to whitecapping, it becomes significant where the waves shoal abruptly due to steep bottom topography. In contrast, directional spreading keeps wave heights in the main channel significantly less than local equilibrium. The wave disequilibrium in the deep navigational channel explains why the marked increase in depth by dredging of the modern channel has had little impact on wave conditions.

Plain Language Summary Heterogeneous, sharply varying bathymetry is common in many coastal regions, and complex interactions between the bathymetry and wavefield affect the amplitude of wave energy that impinges on the shoreline. The manuscript has focused on the formation of waves over complex bathy under different fetch conditions. In addition, the role of channel deepening on wave energy will be of particular interest and discussed in this manuscript. We found that bathymetric change due to dredging has had minimal impact on wave climate because the directional spreading keeps wave heights in the main channel significantly less than local equilibrium.

1. Introduction

Determining the process of wind wave generation, growth, and dissipation in coastal environments is critical to many scientific and engineering applications. Prior studies have focused on the prediction of the wind-generated waves in deep water of the open ocean (Hasselmann et al., 1973; Massel, 1996; Pierson & Moskowitz, 1964) and in water of finite, uniform depth (Hwang, 2006; Young & Babanin, 2006; Young & Verhagen, 1996a, 1996b; Zakharov, 2005). The Pierson-Moskowitz spectrum, developed from measurements in the North Atlantic, presented the distribution of wave energy with frequency in deep water for a fully developed sea (Pierson & Moskowitz, 1964). It assumed that wave energy eventually reaches an equilibrium condition if the wind blows steadily over a sufficient distance. The distribution of wave energy was further defined by the JONSWAP (the Joint North Sea Wave Project) spectrum in fetch-limited conditions within the ocean. The peak of the wave energy spectra becomes more pronounced as waves continue to grow with time and reaches a state of fully developed equilibrium (Hasselmann et al., 1973). In comparison to results from deepwater conditions, both the growth of total wave energy and the migration of the peak frequency to lower values are reduced in water of finite depth (Young & Babanin, 2006; Young & Verhagen, 1996a, 1996b). These physical processes have been incorporated into spectral wave models, for example, SWAN (Simulating Wave Nearshore; Booij et al., 1999), in which the spectral balance of wave action density accounts for refractive propagation and energy dissipation over arbitrary bathymetry. The computational results of

SWAN have been compared with field observations under fetch-limited, depth-limited conditions from Lake George, Australia (Booij et al., 1999; Young & Verhagen, 1996a, 1996b; van der Westhuysen, 2010) and with a number of studies from shallow Dutch lakes (Bottema et al., 2003; De Waal, 2002; Holthuijsen et al., 2008). Although the spectral development of waves over relatively uniform bathymetry has been well documented, the effects of heterogeneous, sharply varying bathymetry on the generation and dissipation of wind waves have received less attention.

Heterogeneous, sharply varying bathymetry is common in many coastal regions, and complex interactions between the bathymetry and wavefield affect the amplitude of wave energy that impinges on the shoreline. In wetlands, the wave energy at marsh edge is a key factor affecting sediment resuspension, marsh edge erosion, and wetland losses (Green & Coco, 2007, 2014; Karimpour et al., 2013, 2016; Marani et al., 2011). For example, on the Atlantic coast of the southern Delmarva Peninsula, marsh retreat rate was linked to wave forcing at marsh edges based on results from a coupled wave-circulation modeling system (Mariotti et al., 2010; McLoughlin et al., 2015). Model cases with different wind conditions showed that wave energy at the boundaries of that marsh was sensitive to wind direction due to fetch limitation. In Chesapeake Bay, significant wave heights were also found to be highly correlated with the local wind speeds and limited by fetch (Lin et al., 2002; Sanford & Gao, 2018). Other factors may affect the distribution of wave energy, including offshore forcing from oceanic swell. A study of Delaware Bay by Kukulka et al. (2017) using a spectral wave model with realistic waves and wind forcing showed that oceanic swell from the continental shelf was the dominant source of wave energy in the mouth and lower bay region. The study showed that wave direction in the bay entrance was altered by bathymetric refraction, which leads to a misalignment between wind and wave directions in the lower bay.

In addition to natural geomorphic variability, many estuaries have experienced significant changes in bathymetry associated with human development and modification for navigation. For example, studies in some estuaries on the Atlantic coast of Europe have found that channel deepening for navigation can modify estuarine hydrodynamics with implications to tidal wetlands (Abbot & Price, 1994; Chernetsky et al., 2010; Talke et al., 2009). The change of shoreline configuration was shown to be associated with an increase of tidal prism and the rate of landward retreat (Cox et al., 2003). Many estuaries have experienced increased rates of shoreline retreat (Mariotti & Fagherazzi, 2013; Sanford & Gao, 2018), and one hypothesis to explain this is that depth increases associated with dredging have changed wave characteristics in the deepening channel (Liria et al., 2009) and enhanced wave energy at the shoreline. Understanding the resiliency of estuarine environments therefore requires both an understanding of the wave processes under changing climate conditions and a quantification of the impact of human-induced changes in morphology that may affect the wave dynamics.

This study examines the dependence of wave conditions in an estuary on local and remote forcing, using observations and modeling to understand how bathymetry and shoreline configuration impact wave generation and dissipation. A numerical model is evaluated against observed waves during calm and energetic wind conditions at multiple locations, including in the navigation channel, along the channel flanks, and in the shallow subtidal near the marsh edge. We use a numerical model with realistic bathymetry to characterize the role of heterogenous bathymetry along with more idealized model forcing scenarios to diagnose processes. An overview of the field observations and numerical model is discussed in section 2. The mechanisms controlling the generation, propagation, and dissipation of wave energy over complex bathymetry are evaluated in section 3. In section 4, the numerical model is used to assess the linkage between incident wave energy flux and observed shoreline retreat, and to quantify the effects of channel deepening on the wave energy distribution.

2. Methods

2.1. Field Observations

The Delaware Estuary is located on the Mid-Atlantic coast of the United States, bordered by the states of New Jersey on the east and Delaware on the west. The estuary consists of a wide lower bay (maximum width 40 km) and a narrower ($<$20 km) region in the middle and upper estuary (Figure 1a). The channel flanks are wide and shallow, generally less than 5-m depth (Figure 1b). Navigation in the Delaware Estuary is facilitated by an approximately 220-km-long channel, dredged to 16-m depth, that extends from near the mouth to the head of tide at Trenton, New Jersey. Observational time series used to evaluate the model performance were collected in 2014 at multiple locations in the middle of the estuary. Wave gauges (Figure 1b) were

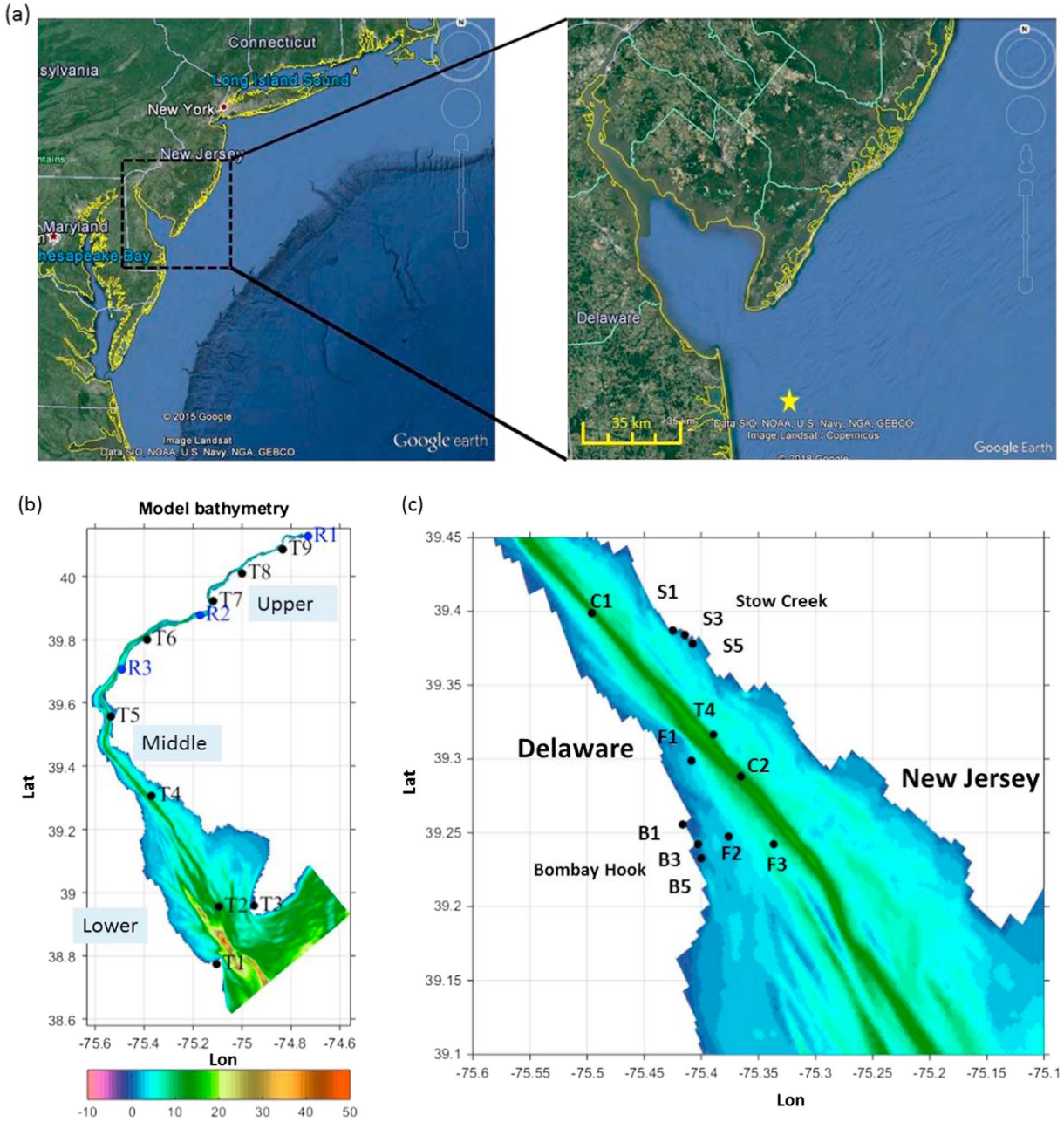

Figure 1. (a) The site location relative to a broader geographic region superposed on a Google Earth image. The location of the wave buoy NOAA #44009 is marked by a star sign. (b) The computational domain bathymetry (color contours, scale on the bottom) with locations of tidal gauges in the two sides of river mouth (T1 and T3) and along the dredged navigation channel (T2–T9). Freshwater discharge was input based on the observed Delaware River discharge at Trenton, NJ (R1). Additional freshwater inputs were included for the Schuylkill River (R2) and Brandywine Creek (R3). (c) An expanded view in the middle estuary with locations of wave gauges along the dredged navigation channel (C1 and C2), two sides of flanks (F1, F2, and F3), and the edge of tidal marsh (Bombay Hook: B1, B3, and B5, and Stow Creek: S1, S3, and S5).

deployed in the channel (C1 and C2), on the shallower flanks (F1, F2, and F3), and immediately offshore of the marsh edge on both sides of the estuary (B1, B3, and B5 on the west near Bombay Hook and S1, S3, and S5 on the east near Stow Creek, each less than 2-m water depth). Acoustic Doppler profilers (Nortek AWAC and RDI ADCP) were deployed at the deeper sites, and high-frequency pressure recorders (RBR Solo/Virtuoso) were used at the marsh edges. Wind data were collected from the center of the estuary at Ship John Shoal, NJ (NOAA #8537121, T4 in Figure 1). Water levels were collected from multiple NOAA tidal gauges, including Lewes, DE (NOAA #8557380, T1 in Figure 1) and Cape May, NJ (#8536110, T3) on the north and south sides

of the estuary mouth, and along the dredged navigation channel at Brandywine Shoal Light, DE (#8555889, T2), Ship John Shoal, NJ (#8537121, T4), Delaware City, DE (#8551762, T5), Marcus Hook, PA (#8540433, T6), Philadelphia, PA (#8545240, T7), Tacony-Palmyra Bridge, NJ (#8538886, T8), and Burlington, NJ (#8539094, T9).

2.2. Model Setup

The model grid bathymetry for the Delaware Estuary was developed based on a composite of archived National Ocean Service bathymetric soundings for the greater estuary (National Oceanographic and Atmospheric Administration, 2014) and U.S. Army Corps of Engineers bathymetry for the recently deepened (to a mean depth of 14 m) navigation channel (United States Army Corps of Engineers, 2014). Most of the survey data from NOAA in the deeper parts of the estuary were collected after 2000, but older soundings were used in shallow areas that had not been surveyed more recently. The domain extends from 50-km offshore of the mouth of the bay to the head of tide at Trenton, NJ, with 20 sigma levels vertically and horizontal grid resolution varying from 300 m in the lower bay to 60 m in the middle of the estuary.

To simulate conditions prior to the start of major dredging projects, historical bathymetric soundings were digitized from the "Map of Delaware Bay and River" published in 1848 by the Survey of the Coast of the United States (USCS) at a scale of 1:80,000. The charted soundings were collected during surveys in 1840–1844 using the lead-line method. Digitized soundings (9,828 total) were entered into GIS and projected to Delaware State Plane coordinate system, and then converted to meters from mean tide level using tidal datum offsets for stations located along the estuary. The soundings were gridded at 10-m cell size for interpolation to the model grid.

The Coupled-Ocean-Atmosphere-Wave-Sediment Transport Modeling System (Warner et al., 2010) was utilized to combine circulation and wave models and to account for the effects of changing water levels and mean currents on the waves over heterogeneous, sharply varying bathymetry. The Regional Ocean Modeling System circulation model solves the simplified Reynolds-Averaged Navier-Stokes equations using the hydrostatic and Boussinesq approximations (Chassignet et al., 2000; Haidvogel et al., 2000). SWAN (Booij et al., 1999) is a spectral wave model that solves the wave action balance equation.

The period of simulation with realistic forcing corresponded with the observations made October to December 2014. Sea surface elevation at the open boundary was forced using tidal constituent amplitudes and phases from the ADCIRC tidal database (Luettich & Westerink, 1992). To simulate storm surge due to remote forcing, the low-pass-filtered sea surface elevation observed at T1 (Lewes DE, NOAA station 8557380) was added to the tidal water level at the open boundary (Figure 2a). Freshwater discharge was input based on the observed Delaware River discharge at Trenton, NJ (see R1 in Figure 1a; USGS #01463500, mean discharge of 314 m^3/s in 2014). Additional freshwater inputs were included for the Schuylkill River (see R2 in Figure 1a; USGS #01474500 at Philadelphia, PA, mean discharge of 90 m^3/s in 2014) and Brandywine Creek (see R3 in Figure 1a; USGS #01481500 at Brandywine River at Wilmington, mean discharge of 19 m^3/s in 2014).

Significant wave height, peak period, and wave direction observed at a NOAA buoy located 10-km offshore of the open boundary (NOAA#44009, 30.5-m depth and 26 NM southeast of Cape May, NJ, see Figure 1a for the location) were used for boundary forcing assuming the JONSWAP spectral wave distribution (Figure 3). Observed wind speed and direction at a middle estuary mooring (T4, NOAA #8537121; Figure 2a) were used to apply spatially uniform wind forcing for SWAN.

2.3. Model Evaluation

In the circulation model, the bottom friction length scale (z_0) was adjusted in the calibration process through comparison to observations, as detailed in the next section. Similarly, calibration of the wave model to observations was done through the bottom friction coefficient C_{bottom}. The dissipation due to whitecapping was parameterized primarily through a dependence on the spectral saturation, which is closely related to wave steepness (van der Westhuysen et al., 2007). The saturation level was calibrated by fetch-limited waves observed at Lake George (van der Westhuysen et al., 2007; Young & Verhagen, 1996a, 1996b). The spectral saturation is a function of wave steepness square in shallow water. A constant breaker steepness threshold $\gamma = 0.73$ was used based on laboratory and field experiments in which the steepness threshold was found to vary between 0.6 and 0.83 with an average of 0.73 (Battjes & Stive, 1985).

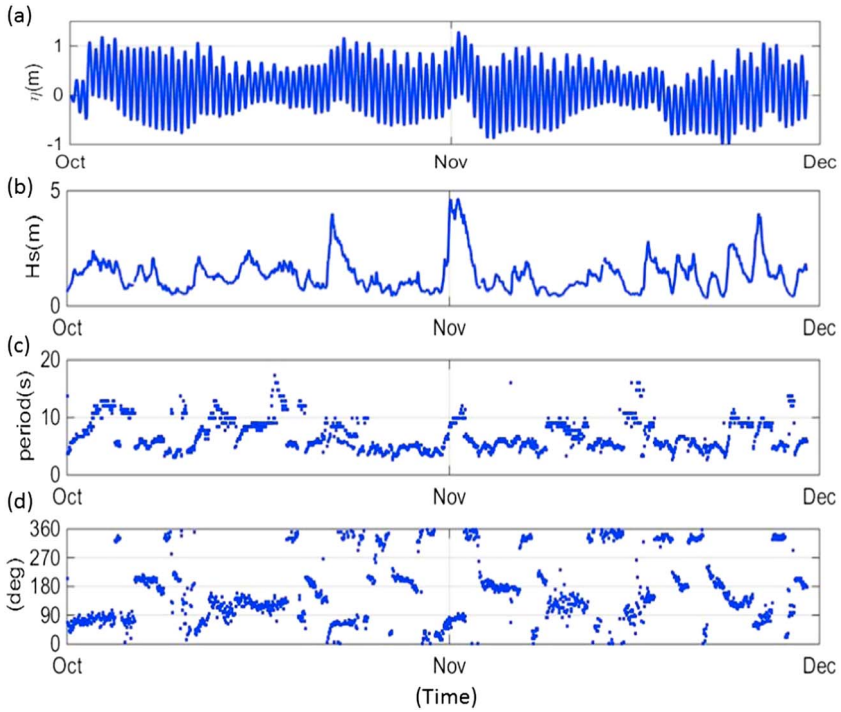

Figure 2. (a) The time series of sea surface elevation at the tidal boundary based on harmonic constituents and low-pass-filtered observations at T1, Lewes, DE (NOAA #8557380; see Figure 1b for the location). (b) The time series of significant wave heights, (c) peak periods, and (d) wave direction observed at NOAA buoy #44009 (30.5-m depth; see Figure 1a for the location), which are applied at the wave model open boundary.

The model accuracy of predicting tidal surface elevation and significant wave height was assessed with the model skill score (SS; Murphy, 1988), which normalizes the difference between the model and observations by the standard deviation of the observations. The maximum SS is 1, and a SS of 0 indicates that the model provides equal predictive skill to the mean of the observations. The maximum SS is equal to the coefficient of determination (r^2), and skill is reduced from r^2 for mismatches in the mean or slope of the regression. The model SSs, slope of the regression (m), and r^2 for water surface elevation and significant wave heights are summarized in Tables 1 and 2.

Bottom roughness (z_0) in Coupled-Ocean-Atmosphere-Wave-Sediment Transport Modeling System was adjusted to maximize model skill for water surface elevation. Except at T8 and T9 in the upper tidal river, the predicted water surface elevation had $r^2 > 0.8$ and regression slopes close to 1 using $z_0 = 0.1$ cm. At T8 and T9 maximum skills were found using $z_0 = 0.5$ cm, possibly owing to spatial heterogeneity in seabed properties. In this study, a spatially uniform bottom roughness of $z_0 = 0.1$ cm is applied, similar to the values used in previous estuarine circulation modeling studies (Lin et al., 2002; McSweeney et al., 2016; Warner et al., 2005). The z_0 for our model is slightly lower than used for a previous modeling study of the Delaware Estuary that used a coarser resolution grid (McSweeney et al., 2016), which is consistent with a study of the Connecticut River estuary that found that z_0 decreased as model resolution increased (Ralston et al., 2016).

The bottom friction coefficient C_{bottom} in SWAN was adjusted to maximize model skill for significant wave height. The dissipation due to bottom friction S_{bot} based on the model of JONSWAP (Hasselmann et al., 1973) is represented as

$$S_{\text{bot}}(\sigma,\theta) = -C_{\text{bottom}}\frac{\sigma^2}{g^2\sinh^2(kh)}E(\sigma,\theta) \quad (1)$$

where C_{bottom} is a bottom friction coefficient (Bouws & Komen, 1983; Hasselmann et al., 1973). Using a spatially uniform $C_{\text{bottom}} = 0.067$ m^2/s^3 as recommended by Bouws and Komen (1983), the simulated significant

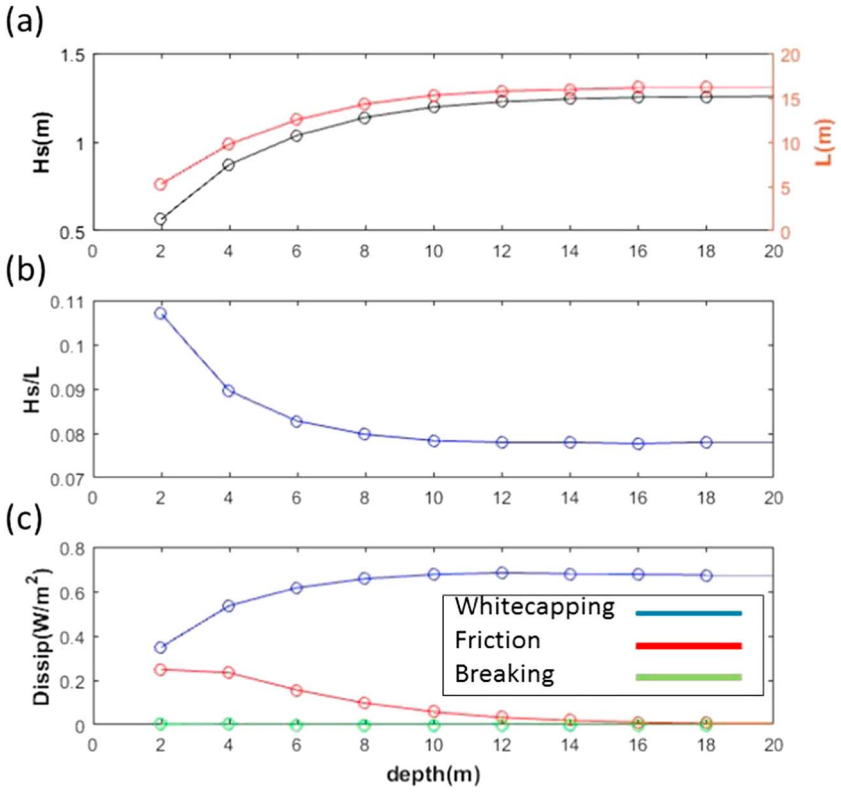

Figure 3. (a) Simulated equilibrium wave height and wavelength, (b) simulated wave steepness, and (c) rate of energy dissipation (whitecapping, bottom friction, and depth-induced breaking) from shallow to deep water in 5-km (blue dots) width channel for 15-m/s winds. These idealized cases in 5-km width channel were used to determine equilibrium wave height (based only on depth dependence) for 15-m/s winds (Figure 8c).

wave heights had reasonable agreement with the measurements in the channel and on shallower flanks in the middle estuary. However, with this C_{bottom}, the simulated significant wave heights were twice as large as observed near the coastline at Bombay Hook (B1) and Stow Creek (C1).

To improve the fit with the observations, the wave model used a spatially variable bottom friction coefficient, C_{bottom} (equations (2)–(4)). The spatially variable bottom friction coefficient formulation (Madsen et al., 1988; Weber, 1991a, 1991b) depends on the bottom orbital motion (U_{rms}) and a nondimensional friction factor f_w:

$$C_{bottom} = f_w \frac{g}{\sqrt{2}} U_{rms} \tag{2}$$

Table 1
Model Skill Score (SS), Slope of Regression (m), and Coefficient of Determination (r^2) for Surface Elevation

Sensor ID	NOAA tidal station name	Model skill (SS)	Slope of regression (m)	Coefficient of determination (r^2)
T1	Lewes, DE	0.96	1.15	0.96
T2	Brandywine Shoal Light, DE	0.95	0.84	0.96
T3	Cape May, NJ	0.94	0.98	0.96
T4	Ship John Shoal, NJ	0.91	0.95	0.92
T5	Delaware City, DE	0.87	0.96	0.90
T6	Marcus Hook, PA	0.75	1.01	0.81
T7	Philadelphia, PA	0.73	0.90	0.81
T8	Tacony-Palmyra Bridge, NJ	0.56	0.84	0.67
T9	Burlington, Delaware River, NJ	0.43	0.81	0.58

Table 2
Model Skill Score (SS), Slope of Regression (m), and Coefficient of Determination (r^2) for Significant Wave Height

Sensor ID	Instrument type	Model skill (SS)	Slope of regression (m)	Coefficient of determination (r^2)
C1	Nortek AWAC	−0.16	0.50	0.33
F1	RDI ADCP	0.36	0.84	0.70
F3	RDI ADCP	0.59	0.70	0.72
BH1	RBR Solo/Virtuoso	0.09	0.61	0.20
SC1	RBR Solo/Virtuoso	−0.08	0.11	0.11

The bottom orbital velocity is calculated as

$$U_{\mathrm{rms}} = \int_0^{2\pi}\int_0^{\infty} \frac{\sigma^2}{g^2 \sinh^2(kh)} E(\sigma,\theta) d\ \sigma d\ \theta \tag{3}$$

and the friction factor f_w is estimated with Jonsson's formulation (1966; cf. Madsen et al., 1988):

$$\frac{1}{4\sqrt{f_w}} + \log_{10}\frac{1}{4\sqrt{f_w}} = m_f + \log_{10}\frac{a_b}{K_N} \tag{4}$$

in which $m_f = -0.08$, a_b represents the near bottom excursion amplitude (Jonsson, 1980), and K_N is the Nikuradse roughness length scale and is related to the log-layer bottom roughness as $z_0 = K_N/30$ (Nikuradse, 1933). As seen in equations (1) and (3)a, decreasing water depth can greatly increase the bottom friction dissipation. A spatially variable bottom friction coefficient C_{bottom} based on Nikuradse roughness $K_N = 0.05$ m (Padilla-Hernández & Monbaliu, 2001; Keen et al., 2007) was used in this study, corresponding with a $z_0 = 0.17$ cm, which is similar to the value of 0.1 cm used in the circulation model. At the wave gage (F3) nearest to the wind data sensor (T4) the resulting SS for significant wave height was 0.59, slope was 0.70, and r^2 was 0.72 (Table 2). SSs were lower at other sensor locations, but overall, the time series of modeled wave height had reasonable agreement with the observations during energetic wind conditions (see next section).

2.4. Idealized Model Setup and Results

In addition to the simulations using realistic bathymetry and forcing (see next section), idealized wave model simulations were evaluated to calculate equilibrium wave height for constant wind speed and range of values of uniform, finite water depth. The range of water depths evaluated (2–18 m) in idealized domains span typical depths in the Delaware Estuary, and the wind forcing (15 m/s) is selected for comparison with conditions during strong wind events (e.g., 2 November 2014 0:00 GMT). The idealized domain is a long channel (>100 km) of uniform depth and width (5 km) to remove the effects of bathymetry heterogeneity on the wavefield. From the asymptotic wave heights in the channel we develop a relationship between channel depth and equilibrium waveheight for a given wind forcing. The asymptotic wave height from this idealized model configuration with water depth of 2 m compared well against the measurements from Lake George, Australia, with similar mean depth (Young & Verhagen, 1996a, 1996b). Those measurements have been used to develop a set of equations relating wave amplitude to fetch and depth (Young & Verhagen, 1996a, 1996b) that have been applied to several studies in fetch-limited, depth-limited conditions over relatively uniform bathymetry (Mariotti & Fagherazzi, 2013; Sanford & Gao, 2018). Results from the idealized, uniform channel SWAN simulations in this study are summarized here and later used to help interpret the Delaware Estuary simulations with realistic forcing and heterogeneous bathymetry.

Model cases were run using water depths from 2 to 18 m in increments of 2 m, and equilibrium wave heights were determined from the asymptotic wave height in the downwind region. Comparing the idealized channels with water depths of 2 to 4 m, equilibrium wave height increases from 0.56 to 0.87 m. In cases with deeper channels the incremental wave growth is more modest, increasing from 1.42 to 1.46 m from 12- to 14-m depth (blue curves, Figure 3a). The idealized channel results were used to quantify the relationship between depth and equilibrium wave height (Figure 3a). This relationship was used to calculate the spatial distribution of equilibrium wave height (limited only by depth) in the Delaware Estuary based on local bathymetry for 15-m/s winds (Figure 8c), which is compared with the wavefields calculated using realistic forcing conditions. In the idealized, uniform channel cases, whitecapping, which limits the wave height through the steepness

constraint, is the dominant mechanism for dissipation (Figures 3b and 3c). Friction only becomes important at depths less than 6 m, but even at 2-m depth it is less important than whitecapping for the equilibrium solution. As will be shown in the simulations with realistic forcing, friction can locally become more important than whitecapping in certain nonequilibrium conditions. In shallow water cases ($<$6 m), the whitecapping dissipation decreases despite an increase in wave steepness, but this is due to the decrease in wave height and total wave energy in shallow water as a result of the increased dissipation by bottom friction. For the range of depths considered in this idealized case, wave breaking is never an important dissipation mechanism. However, note that it becomes dominant in the surf zone, which it not resolved in the Delaware simulations.

To further examine the dependence of wave height on channel width, idealized simulations were run for 15-m/s winds with 16-m water depth and different widths of 5, 2, and 1 km. The resulting wave heights decrease from 1.13 to 1.01 m (11%) as channel width decreases from 5- to 2-km width, and from 1.01 to 0.85 m (19%) from 2- to 1-km width. Comparing the wave heights in narrower channel (1 km) for different water depths, equilibrium wave height increase from 0.49 to 0.64 m from 2-m to 4-m depth, but the wave height increases for deeper channels were minimal, remaining at 0.75 from 12 m and deeper channels. This can be explained by the strong influence of width on wavelength, which in turn limits the wave height through the steepness constraint on whitecapping. Although wave steepness is slightly greater in the narrower channel cases, wave heights in the narrower channel cannot equilibrate with the full channel depth. In addition, the difference between incident wave direction and wave direction at the edges of the channel increases as channel width decreases due to directional spreading of wave energy, which transfers energy from the center toward the edges of the channel.

3. Results of Realistic Domain Simulations

3.1. Observed and Simulated Wave Conditions

During November 2014, winds in the central Delaware Estuary were up to 15 m/s from the north and typically 5 m/s or less during southerly wind conditions (Figure 4). During periods of strong wind from both north and south, observed wave heights increased in the middle estuary (Figure 4c) and offshore (Figure 4d). The correspondence between local winds and wave height in the estuary suggests that local forcing is one of important factors for the wave conditions in the middle estuary, but the coincident increase in offshore wave height leaves open the possibility of remote inputs. We will address the relative contributions of local and remote forcing using model cases.

As an example of conditions during the observations with strong wind forcing, Figure 5a shows the spatial distribution of simulated significant wave heights during a strong northerly wind event (2 November 2014 0:00 GMT). The wind was 15 m/s from the north and the buoy offshore recorded 4.5-m significant wave height from the east (Figure 2). The simulated significant wave heights at this time were less than 0.5 m in the upper estuary, around 0.8 m in the middle estuary, and up to 1.5 m in the lower bay. Similar spatial gradients were seen frequently in both the observations and the model, with the most energetic waves typically occurring in the central lower bay. At 2 November 2014 0:00 GMT, the observed and simulated significant wave heights during this wind event were 1 m in the navigation channel (14-m water depth, C1, Figure 5b) and 0.8 m on the shallower western flank (4.3 m, F1, Figure 5c). At F3 (5.5 m, Figure 5d), which was slightly deeper than F1, the observed and simulated wave heights were 1 m. At stations in the shallow subtidal ($<$2 m) near Bombay Hook (B1) on the western shore and Stow Creek (S1) on the eastern shore the observed and simulated wave heights were less than 0.6 m.

Based on the observations, significant wave heights were highly correlated with wind speed (Figures 4b and 4c), but near the edge of marsh, wave heights were also modulated by the tidal variation in water level (water depth $<$ 2 m, Figures 5e and 5f). However, in the channel and on the flanks (water depth $>$ 2 m), wave heights in the observations and model were not significantly modulated by tidal variations in water level or current speed (Figures 5b–5d). Previous studies have also found that wave-current interactions do not significantly alter wave conditions in the middle and upper estuary (Kukulka et al., 2017), so for computational efficiency, we use the SWAN model alone to examine how forcing conditions, bathymetry, and geometry contribute to the spatial variation of significant wave heights, including assessing the mechanisms control the generation and dissipation of wave energy. Specifically, we examine how the influence of wave input from the coastal

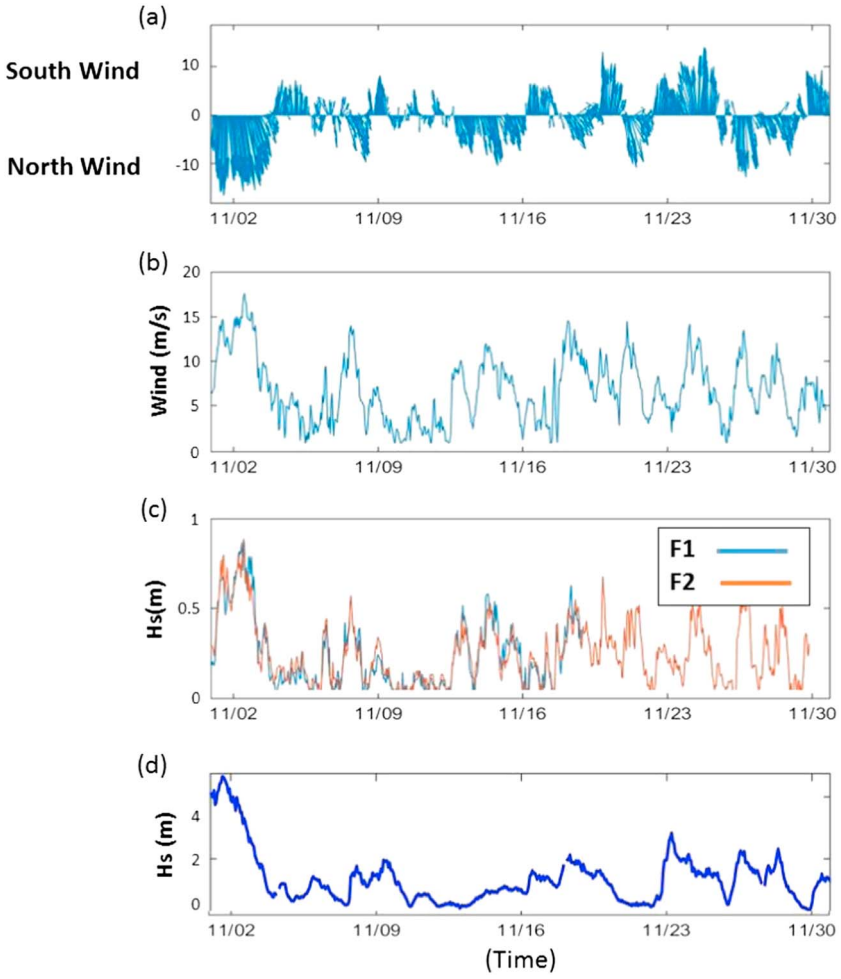

Figure 4. Observed winds and wave height (as significant wave height H_s) during November 2014. Measured (a) wind direction and (b) speed observed at T4 (see location at Figure 2b). (c) Observed waves in F1 and F2 (see Figure 2b for location). (d) The observed waves at NOAA buoy #44009 (30.5-m depth).

ocean varies along the estuary, and how bathymetric heterogeneity leads to significant departures from the wave amplitude that would be expected for wind-generated waves at equilibrium with the local water depth. The patterns of disequilibrium are due to interactions between the bathymetry and the mechanisms of wave energy dissipation, which are quantified in relation to the bathymetric controls.

3.2. Local Versus Remote Wave Generation

One important aspect is the extent to which waves in the estuary depend on the offshore input from the open ocean compared with generation by local winds. Strong winds typically come from the northwest during winter storms and from the south or southeast due to extratropical depressions during the summer. Model tests were run using constant wind forcing and wave boundary conditions to understand the dominant mechanisms that control the distribution of waves in the estuary (Figure 6). As a representative test case, the model was run to steady state with 15-m/s wind from the south and 3-m waves incident from the offshore boundary (Figure 6a). Similar to the realistic forcing result (Figure 5a), the simulated significant wave heights (up to 1.5 m) are greater in the lower bay than those in the middle and upper estuary. The model was also run separately with only wind forcing (Figure 6b) and only remote swell forcing (Figure 6c). The significant wave heights in the upper and middle estuary for the case with only wind (Figure 6b) are similar to the result with both wind and offshore forcing (Figure 6a), indicating that local winds provide the dominant source of energy for waves in the upper and middle estuary rather than offshore wave conditions. In the case with forcing only from the offshore boundary (Figure 6c), the simulated significant wave heights in the

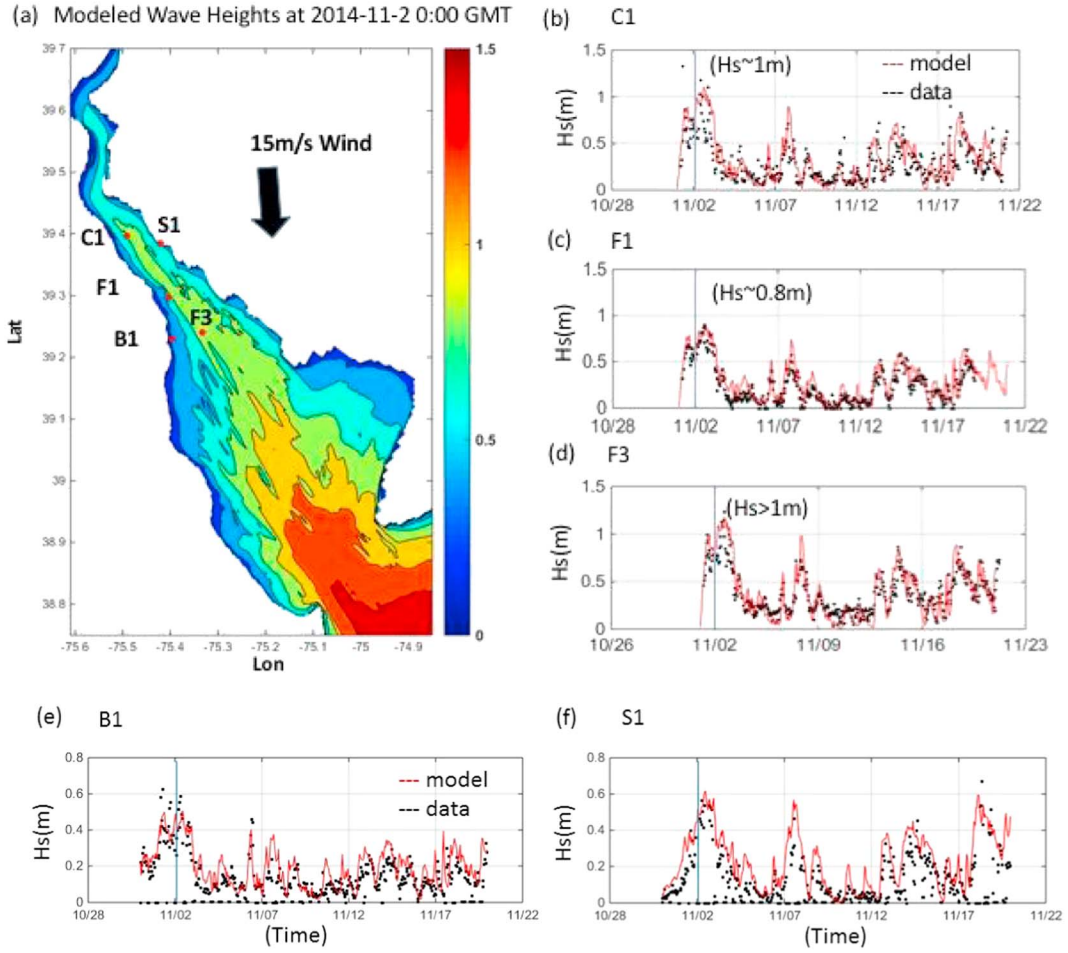

Figure 5. (a) Simulated significant wave heights at 2 November 2014 0:00 GMT. (b–f) Measured and modeled significant wave height time series at C1, F1, F3, B1, and S1.

middle estuary are near zero and in the lower bay waves are smaller by a factor of 2 or more than those with wind forcing (Figure 6a). Kukulka et al. (2017) found that oceanic swells did not penetrate into the lower bay based on idealized simulations and ray tracing experiments. Our model results indicate that the remote wave forcing from the ocean contributes around 20% of total wave height in the lower bay, and up to 40% near the mouth under the conditions representative of a summer storm event (15-m/s wind from the south and 3-m wave normal incident from the offshore boundary, Figure 6d). The influence of offshore forcing to the generation of wave energy in the estuary is limited by the shoaling bathymetry that steepens the long period swell and leads to energy dissipation, and in the middle and upper estuary, waves depend almost exclusively on local winds.

3.3. Influence of Direction of Forcing: Fetch Limitation and Sloping Bathymetry

Wave generation by local winds depends both on the estuarine bathymetry and shoreline configuration and is highly dependent on wind direction. To assess the response of waves in the Delaware Estuary to representative wind forcing, model cases were run with constant, uniform wind forcing at 15 m/s from the northwest (300°) and southwest (145°), conditions frequently observed in the middle of the estuary during winter and summer storm events, respectively (Figure 7). For the northwest wind conditions, the simulated significant wave heights increase from ~0.7 m in the upwind region of middle estuary to >1.5 m in the downwind region of the lower bay (Figure 8a). For the southeast wind forcing condition, the simulated significant wave heights in the center of the lower bay are greater than for the northwest wind due to the extensive fetch from the ocean into the lower bay (Figure 8b). However, the wave heights decrease in the downwind direction for

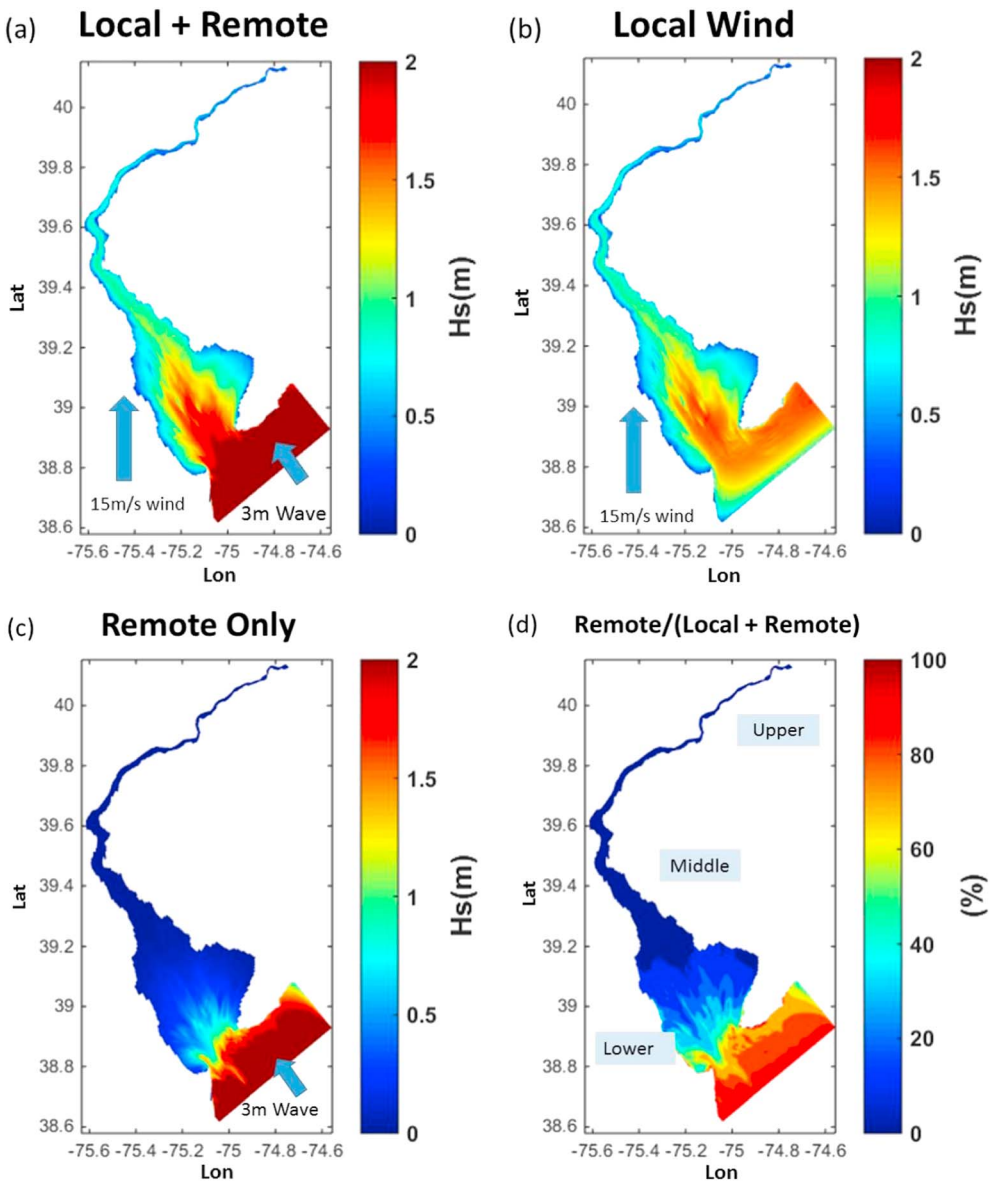

Figure 6. Simulated significant wave heights under the condition of (a) 3-m waves incident from the boundary and 15-m/s wind from the south, (b) only 15-m/s wind, (c) only 3-m waves incident from the boundary, and (d) the contribution of remote wave forcing to the simulated significant wave heights shown in (a).

the southeast case, with typical values in the upper and middle estuary of 0.7 m. The depth-to-equilibrium wave-height relationship developed from the idealized channel cases (Figure 3) was used to calculate equilibrium wave height (limited only by depth) for 15-m/s winds at every location in the estuary (Figure 8c) for comparison with the wavefield resulting from the simulation with realistic forcing.

Differences in the response of the system to wind forcing with equal magnitude but nearly opposite direction highlight the impacts of heterogeneous bathymetry (Figures 8d–8f). The negative values indicate that waves are smaller than equilibrium for the local water depth, and the positive values indicate waves that are greater than the equilibrium value. Discrepancies from equilibrium are due both to fetch limitation that depends on distance from the shoreline in the downwind direction and on steeply sloping bathymetry that changes more rapidly in the downwind direction than the wavefield can adjust.

Under the northwest wind conditions, waves are less than equilibrium height in the western middle estuary due to fetch limitation and only approached equilibrium in the downwind region of the eastern middle

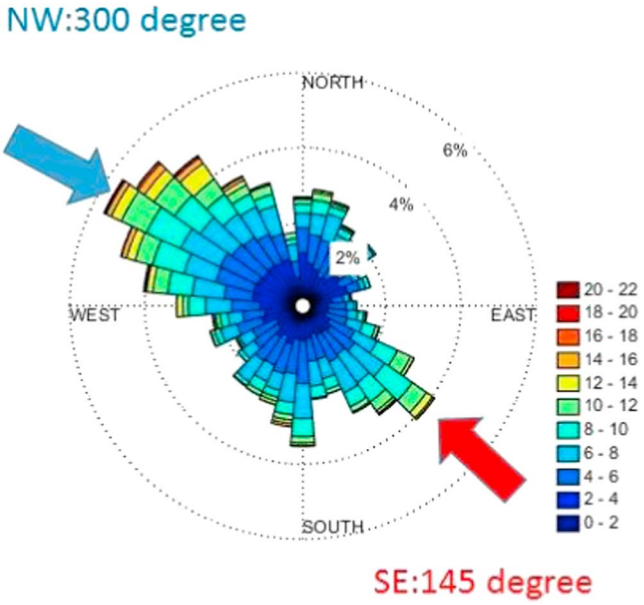

Figure 7. Wind rose based on the observed wind during 1 January to 31 December 2014 at Ship John Shoal. Scale in m/s. The arrows represent wind forcing for idealized cases. Northwest (NW) is the predominant wind direction in winter, and southeast (SE) is predominantly in summer.

estuary and the lower bay (Figure 8d). According to the idealized, uniform channel model results, more than 10 km of fetch is needed to obtain equilibrium waves in 4-m water depth or larger. Correspondingly, waves in the upper estuary are always less than equilibrium height due to fetch limitation. The region of fetch limitation is less extensive for the southeast wind case due to the orientation of the bay. For the southeast wind, the upper estuary is oriented downwind with a fetch of up to 100 km, so wave heights in the upper estuary should be near or greater than equilibrium. However, in the deep navigational channel, wave heights do not equilibrate because directional spreading of wave energy transfers energy away from the center of the channel toward the shallower edges (Figure 8e). Wave heights exceed local equilibrium in much of the lower bay as waves propagate landward with the wind from deeper regions offshore. The rate of wave growth due to shoaling in the lower bay exceeds wave dissipation rates leading to a convergence of wave energy and growth in wave amplitude relative to equilibrium forcing. The same is true for the northwest wind case in the eastern lower bay, where wave heights exceed the local equilibrium depth as waves cross the main channel and propagate into shallower water, shoaling faster than energy is lost due to the wave dissipation mechanisms. Correspondingly, model results averaged over the two wind forcing cases show that wave heights in the middle and upper estuary are always much smaller than equilibrium (Figure 8f). The mechanisms affecting wave growth and dissipation that produce discrepancies from local equilibrium will be discussed in the next section.

3.4. Wave Energy Dissipation

The total wave energy dissipation in SWAN includes the dissipation of wave energy due to whitecapping, bottom friction, and depth-induced breaking. In the idealized, uniform channel cases, whitecapping is the dominant mechanism for dissipation and bottom friction contributed up to 20% to 40% of the total dissipation in shallower channel cases (depth $<$ 4 m). The cases with realistic bathymetry of the Delaware Estuary are consistent with the idealized uniform channel in that for regions of the lower bay deeper than ~10 m, whitecapping is the dominant energy sink with up to 90% of total energy dissipation (Figure 9). Note that depth-induced breaking only is significant in regions adjacent to the shoreline, whereas whitecapping and bottom friction dominate in the rest of the estuary.

Integrated over the entire estuary the energy dissipation due to bottom friction is small relative to whitecapping, but in parts of the domain bottom friction dissipation in the realistic bathymetry case greatly exceeds that in the uniform channel cases with the same depth. As waves move into shallow water and shoal, wave height becomes greater than equilibrium for that water depth, and the near-bottom orbital velocities associated with the anomalously shoaling waves result in locally intensified bottom friction, in some locations exceeding the dissipation due to whitecapping (Figures 9c and 9f). This intensification in bottom friction occurs where the waves shoal abruptly due to steep bottom topography, resulting from the nearly exponential depth dependence of the wave orbital velocity (equation (3)). Intensified friction occurs almost exclusively on the topographic highs associated with the longitudinal shoals, particularly in the lower estuary. The shoaling effect occurs for all wind directions, but it is more pronounced for the southeast wind case, due to the decrease of water depth toward the northwest along the estuary (see Figure 1b). The dissipation rate due to bottom friction and depth-induced breaking becomes equal or greater than whitecapping over the abrupt shoaling ridge in the midestuary, where the averaged slope was around 0.005 (Figures 10a and 10b). The wave dissipation due to bottom friction increases, but whitecapping decreases due to abrupt decreases in water depth. The ratio of dissipation due to bottom friction and whitecapping is related to fetch, wind speed, slope, and water depth (see equations (2)–(4)). A similar example could be found near the entrance of the bay where the wind-induced wave energy was dissipated by the steep, linear ridge where the averaged slope was around 0.01(see Figures 10c and 10d). Different from tidal inlets and bar-build estuaries where depth-induced breaking is the dominant dissipation mechanism, wave energy in the bay entrance was dissipated by the combination of whitecapping and locally enhanced bottom friction over longitudinal shoals.

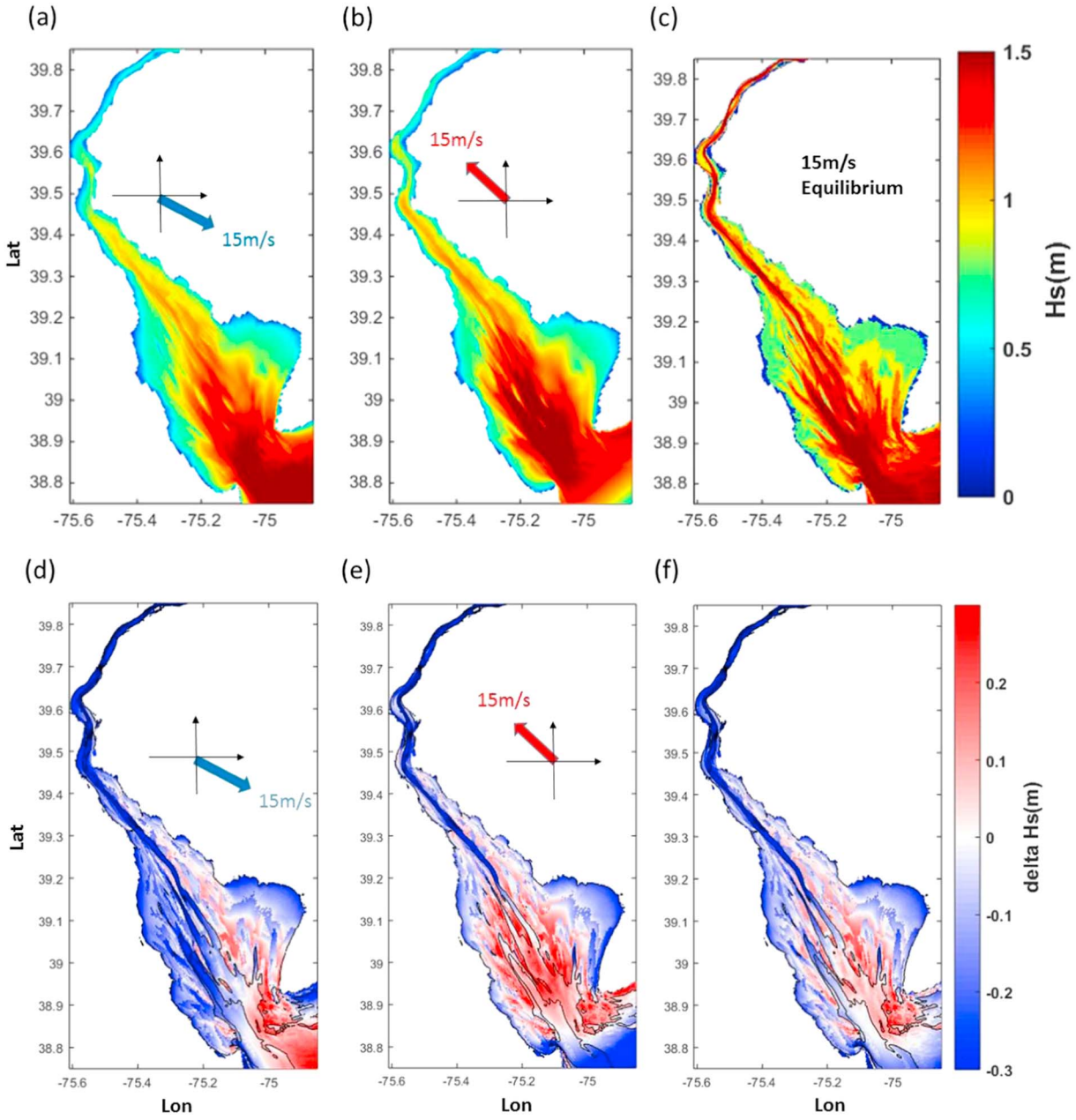

Figure 8. The modeled significant wave heights (the color contours indicate significant wave heights and scale on the right) during (a) northwestern wind and (b) southeastern wind conditions. (c) The spatial distribution of equilibrium wave heights based on local water depth. The difference between simulated and equilibrium significant wave heights during (d) northwest wind, (e) southeast wind conditions, and (f) the average difference between the northwest and southeast wind cases and equilibrium wave heights. The 10-m depth contour is shown in black.

The model results demonstrate that whitecapping-induced energy dissipation is dominant in the estuary channel, while energy dissipation due to bottom friction is focused on longitudinal shoals and channel flanks. Correspondingly, the bottom stresses due to wave forcing are greater (up to 0.4 Pa) on the shallower flanks than in the channel (less than 0.1 Pa; Figure 11). These regions of enhanced frictional dissipation correspond with wave-induced bottom stresses that are more intensified locally than previously found in shallower and more spatially uniform estuaries (Karimpour et al., 2016, 2017; Mariotti & Fagherazzi, 2013; Mariotti et al., 2010). For the northwest wind conditions, the simulated wave-induced bottom stresses increase from around 0.1 Pa in the upwind region of the middle estuary to more than 0.3 Pa in the downwind region of the lower bay. For the southeast wind forcing, the bottom stresses in the lower bay are greater than for the northwest

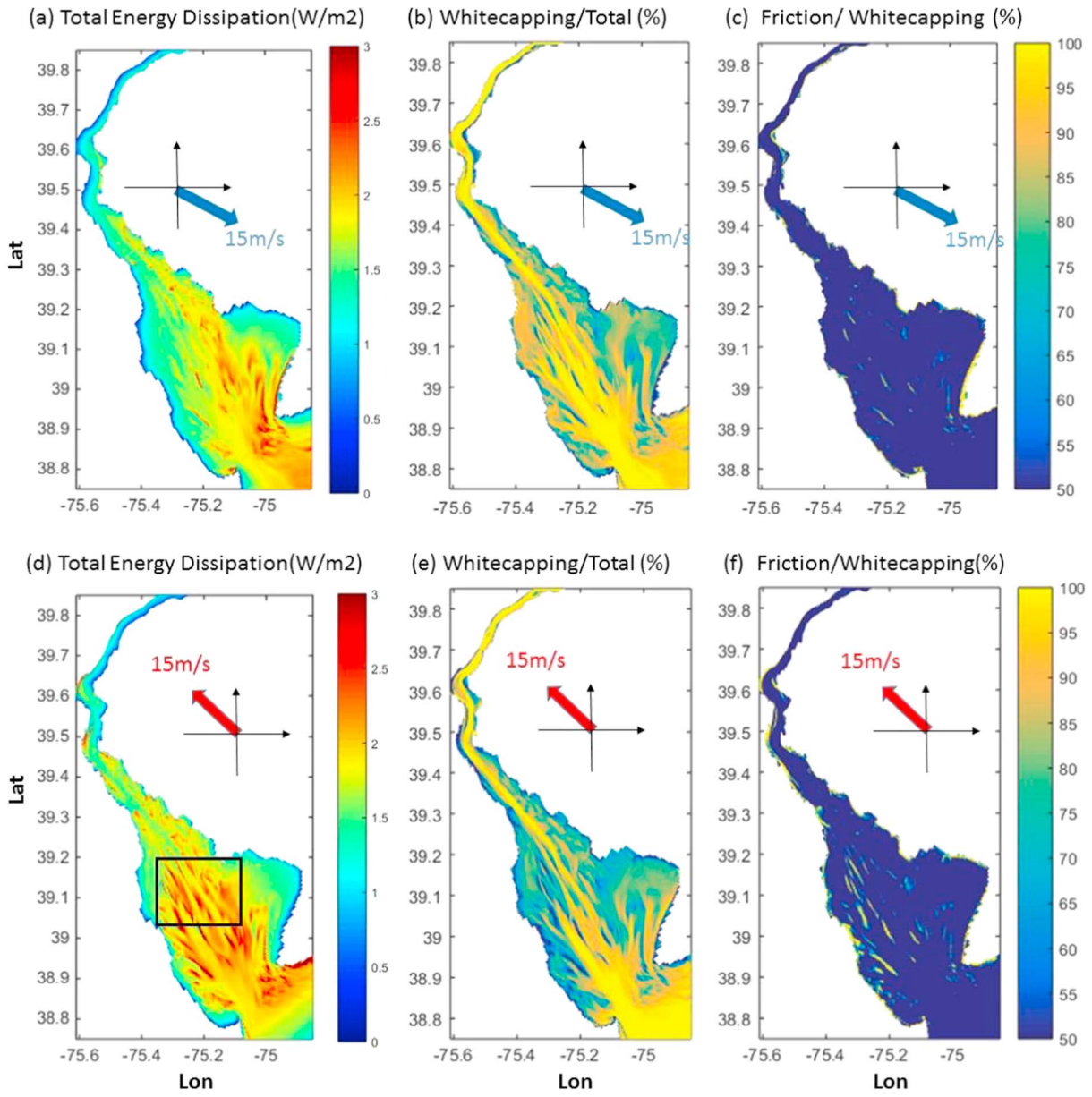

Figure 9. (a) The simulated total wave energy dissipation and the contribution of wave energy dissipation due to (b) whitecapping and (c) bottom friction versus the total energy dissipation during northwest wind conditions. (d–f) The simulated wave energy dissipation during southeast wind conditions.

wind, especially on longitudinal shoals that had enhanced frictional dissipation. In both wind direction cases, the regions of elevated wave-induced stresses correspond to conditions in which waves are propagating into shallower regions with steeply varying bathymetry and where wave heights exceed equilibrium with the local water depths (Figures 8d and 8e).

4. Wave Energy and Shoreline Change

The Delaware Estuary has one of the longest continuous salt marsh systems on the Atlantic coast (Kraft et al., 1992). The coastline of the upper and middle estuary is characterized by eroding brackish marsh, whereas the lower estuary coast (Delaware Bay) consists of a transgressing barrier beach backed by salt marsh (Fletcher et al., 1990). Shoreline mapping has documented rapid rates of coastal retreat along the Delaware Estuary with evidence of increasing rates in recent decades (French, 1990; Maurmeyer, 1978; Phillips, 1986;

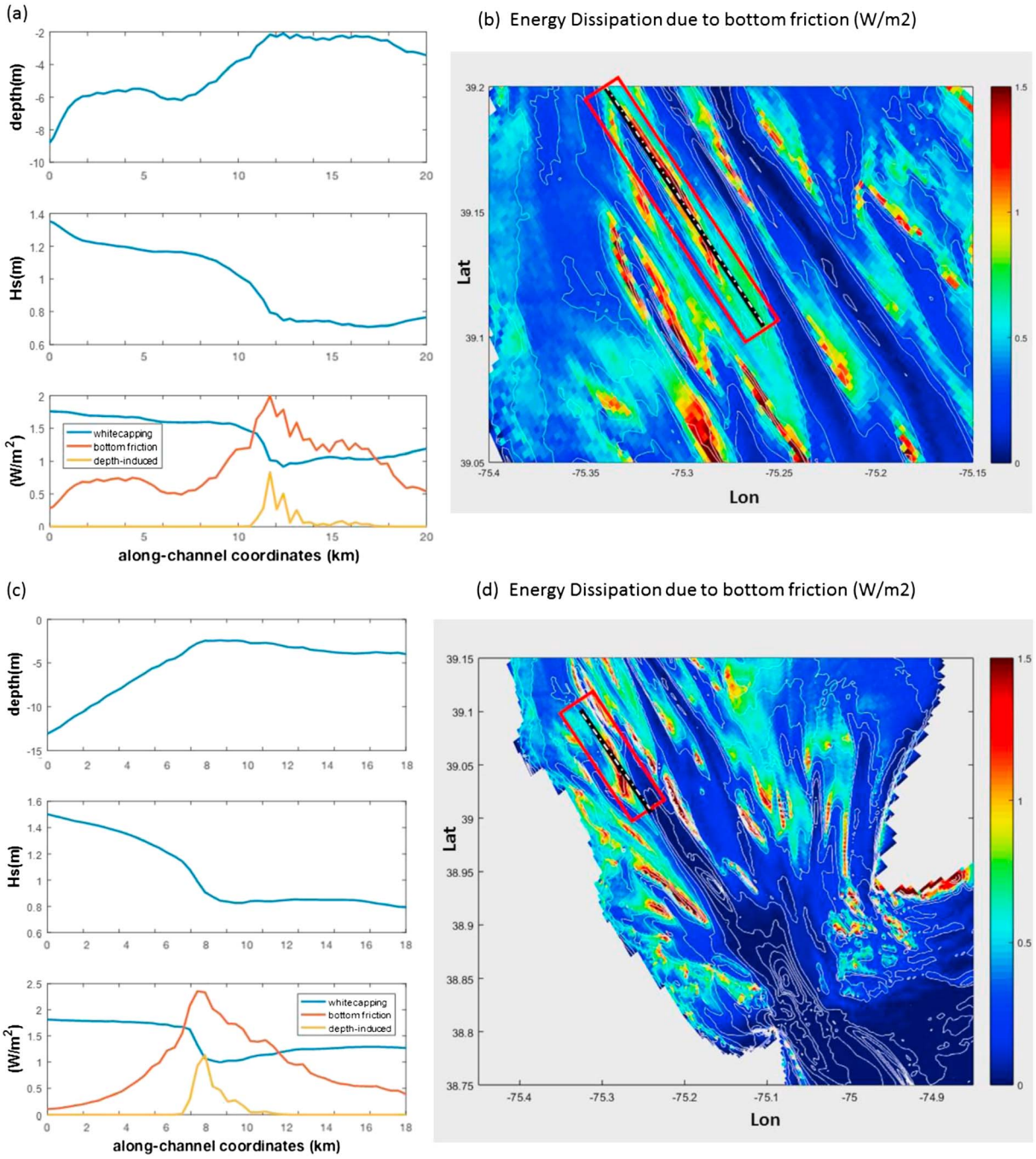

Figure 10. (a) The profile of water depth (upper), wave height (middle), and dissipation rate (lower) due to whitecapping (blue lines), bottom friction (maroon lines), and depth-induced breaking (yellow lines) along the longitudinal ridges during southeast wind conditions. The transect of longitudinal ridges shown in Figure 10a is specified by thick black lines in Figure 10b. (b) The simulated wave energy dissipation due to bottom friction in the lower bay during southeast wind conditions. The location and wind direction are shown in Figure 9d. The 1- to 10-m depth contour (1-m space) is shown in white. Figures 10c and 10d show another profile along the ridge in the entrance of the bay during the same wind condition.

Pijanowski, 2016). Evidence of accelerated shoreline retreat along the tidal wetland coast has raised concerns regarding the sustainability of the extensive brackish and salt marshes (Kearney et al., 2002; Kraft et al., 1992).

4.1. Wave Energy Flux and Shoreline Retreat

Marsh erosion critically depends on the wave energy that reaches the shoreline (Marani et al., 2011; Schwimmer, 2001), and studies have found that incident wave energy flux at the edge of the coastal

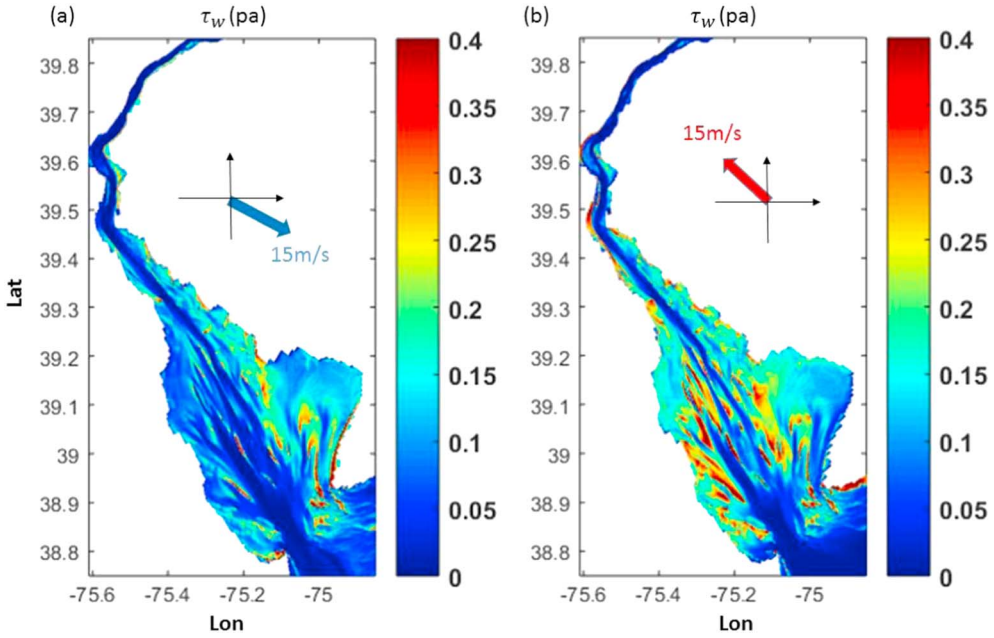

Figure 11. The simulated bottom stresses due to wave forcing (τ_w) during (a) northwest wind and (b) southeast wind conditions.

marsh can be correlated with marsh retreat rates (Mariotti et al., 2010; McLoughlin et al., 2015). In this study, modeled wave heights were validated with observations from wave gauges deployed immediately offshore of the marsh edge on both sides of estuary (B1, B3, and B5 on the west and S1, S3, and S5 on the east, each less than 2-m water depth; Figure 5 and Table 2). From the model results, the incident wave energy flux (or wave power) was calculated at the coast (Karimpour et al., 2016; Mariotti et al., 2010; McLoughlin et al., 2015; Sanford & Gao, 2018) for the characteristic winter and summer storm conditions, the 15-m/s northwest and southeast wind cases (Figures 12a and 12b). The incident wave energy flux in these results is similar in magnitude that in studies of marshes in Rehoboth Bay, lower Delaware (Schwimmer, 2001), and the Delmarva Peninsula (Mariotti et al., 2010).

The simulated incident wave energy flux along the shoreline is greater along the New Jersey coast (in many locations $>$1.0 KW/m) than along the Delaware coast (generally $<$0.6 KW/m). A localized region of intensified wave energy flux is found near Bombay Hook on the Delaware coast, where for southeast wind conditions (e.g., summer storms), the incident wave energy flux is around 1.0 KW/m. In each wind direction case, the coastline areas with elevated incident wave flux are adjacent to regions of the subtidal estuary that have wave heights approximately in local equilibrium with the forcing conditions (Figures 8d and 8e). In contrast, coastline regions with lower incident wave energy flux have wave heights offshore that are typically less than local equilibrium, either because fetch is limited by downwind distance from land or because they are downwind of the sharp longitudinal ridges that remove wave energy through bottom friction dissipation, creating shadow zones of nonequilibrium waves.

The 15-m/s wind cases represent typical winter and summer storm conditions, but to calculate a wave flux that is representative of the longer-term forcing conditions, we ran simulations over a range of wind directions and speeds. The observed winds from Ship John Shoal were binned by direction (12 bins with 30 degree resolution) and speed (4 magnitudes: 5, 10, 15, and 20 m/s; Mariotti et al., 2010; McLoughlin et al., 2015). Based on the observed wind distribution from 2014 (Figure 7) and the 48 different combinations of speed and direction, we calculated the frequency-weighted average incident wave energy (Figure 12c).

The spatial distributions of simulated incident wave energy fluxes were compared with shoreline retreat rates determined by shoreline mapping (Figure 12d) by Pijanowski (2016). In that study, the shoreline retreat rate was based on the Digital Shoreline Analysis System, which computes rate-of-change

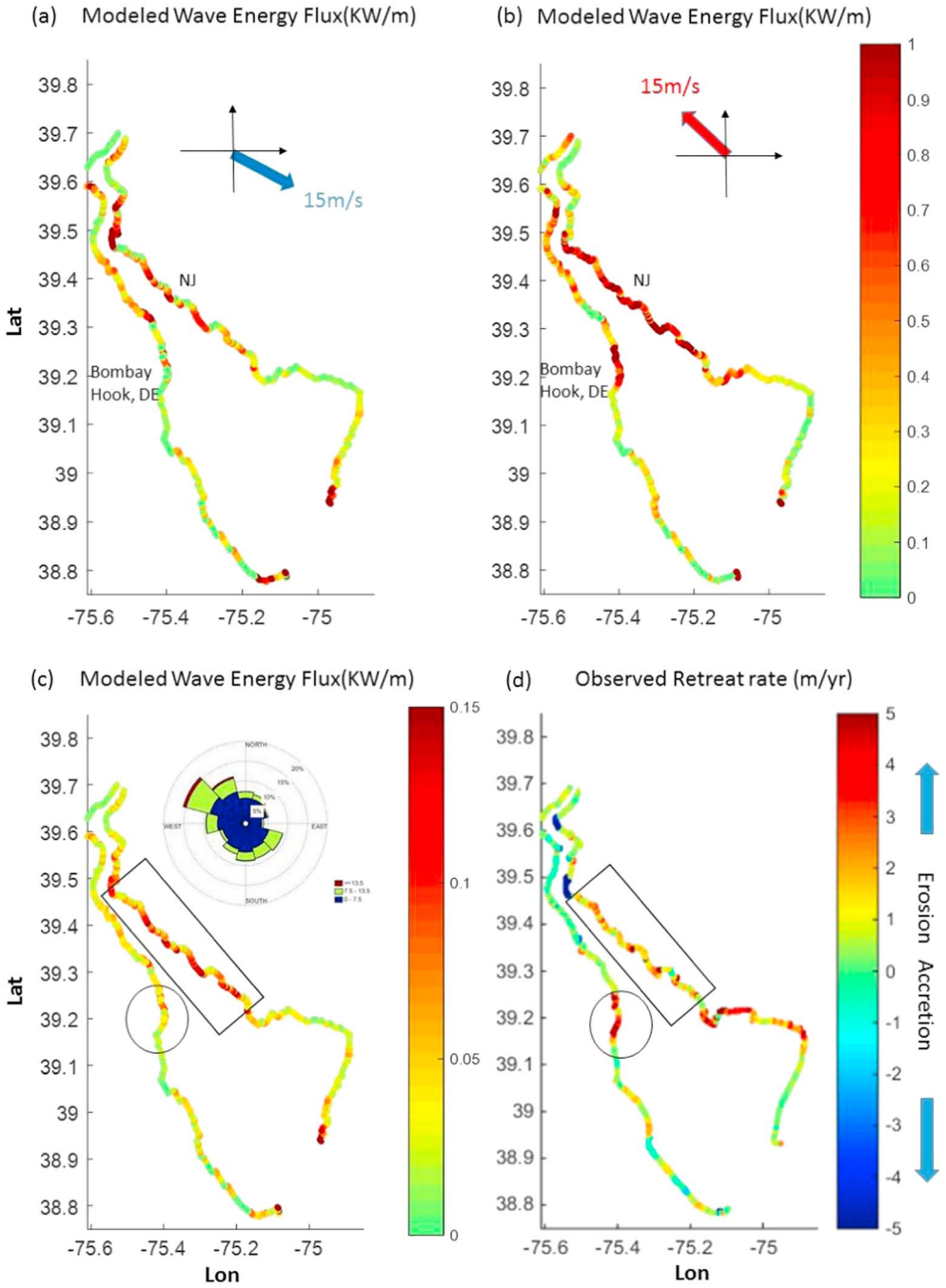

Figure 12. The simulated incident wave energy flux during (a) northwest wind and (b) southeast wind conditions. (c) The simulated incident wave energy flux based on 2014 observed wind statistics. (d) The observed average rate of shoreline retreat (m/year) from 1880 to 2012 (Pijanowski, 2016).

statistics from multiple historical shoreline positions (Thieler et al., 2009). For the lower estuary and bay, shorelines from the periods 1879–1885 (hereafter 1879) and 1943–1948 (1948) were digitized from NOAA topographic sheets. The most recent Delaware shoreline used for this study was constructed from high-resolution (0.3 m, with a root-mean-square error of 0.88 m) USGS orthophotography taken in 2012. Shorelines were defined digitally following the high water level (Boak & Turner, 2005; Crowell et al., 1991). In areas where the high water level was not visible, such as on vegetated wetland coast, the marsh edge was taken as the shoreline.

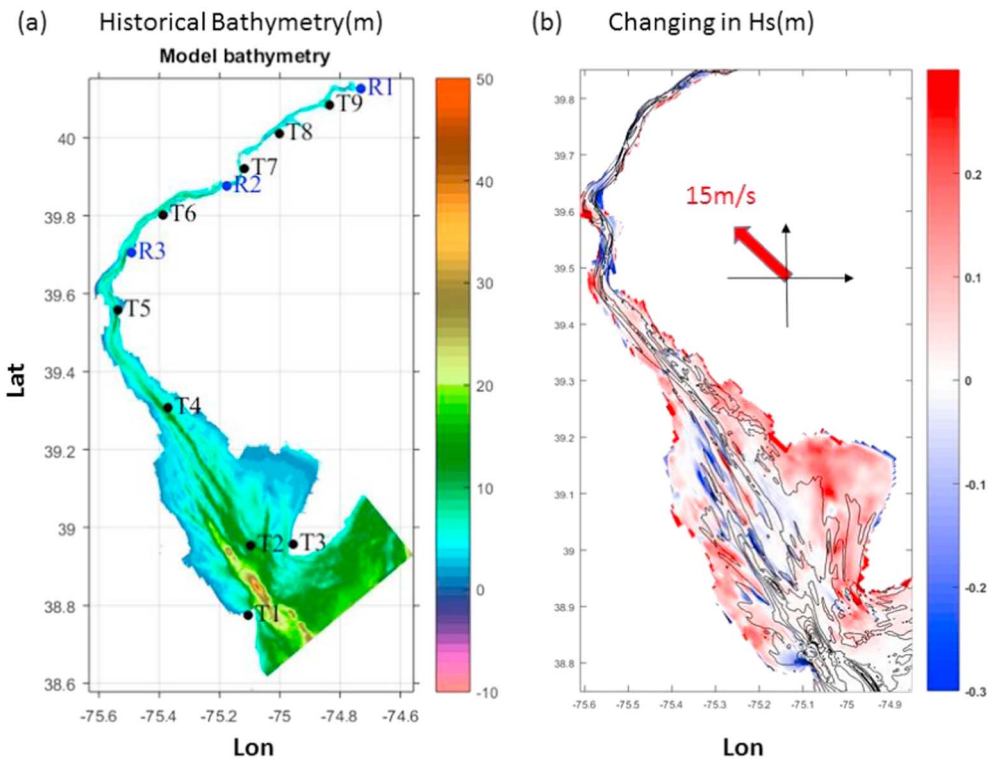

Figure 13. (a) The historical bathymetry for the predredged estuary (color contours, scale on the right) and (b) map of change in significant wave heights (Hs) under southeast wind conditions. The positive values indicate simulated waves over modern bathymetry are greater than those over the historical bathymetry. The 4-, 6-, 8-, and 10-m depth contours are shown in black.

Both the shoreline retreat rates and simulated incident wave energy fluxes are generally greater along the New Jersey coast than those estimated along the Delaware coast. The shoreline retreat rate at Bombay Hook is an exception, where the average retreat rate is up to 5 m/year. The average incident wave energy flux is 0.13 KW/m for the Delaware coast and 0.2 KW/m for the New Jersey coast. Averaged from 1880 to 2012, the regression-based mean rates of change along the Delaware coast are 0.68 and 1.5 m/year along the New Jersey coast (Pijanowski, 2016). In most cases, the regions with more intense wave energy are those with more rapid shoreline retreat.

Whereas generally the model predictions indicate high incident wave energy where the erosion rates are high, there are some exceptions. Along parts of the New Jersey coast of the lower bay, the simulated incident wave energy flux is relatively low, but the retreat rate is high. One source of uncertainty in the wave model, particularly for coastlines adjacent to broad, shallow subtidal regions, is the dependence of the frictional wave dissipation on the Nikuradse roughness K_N (equations (2)–(4)), a parameter that typically ranges from 0.01 to 0.1 m (Keen et al., 2007). The calibration to the measurements in the middle and upper estuary resulted in K_N = 0.05 m, a roughness length that is consistent with ripples on the inner shelf (Padilla-Hernández & Monbaliu, 2001; Keen et al., 2007) but may be less well suited to represent smaller scale roughness features in the shallow parts of the lower bay. For example, for the southwest wind condition and a lower roughness of K_N = 0.01 m the simulated incident wave energy flux along the New Jersey coast of the lower bay increases to around 2.5 KW/m, compared to less than 1 KW/m for the case with K_N = 0.05 m. Nearshore measurements of wave conditions along the New Jersey coast of the lower bay similar to the observations collected here in the middle estuary could help constrain the roughness and provide a more robust spatial representation of incident wave energy flux.

4.2. The Effect of Channel Deepening

In the late 19th century, prior to the era of dredging, the natural depth of the channel in the upper estuary ranged from 5 to 7 m (DiLorenzo et al., 1993). During the early 20th century the channel was progressively

deepened to accommodate larger ships, and by 1945 was 12-m deep. A channel deepening project from 2010 to 2017 increased the controlling depth to 14 m. Rapid shoreline retreat has coincided with the period since deepening of the navigational channel began in the early 1900s (Pijanowski, 2016), and one hypothesis is that the deeper navigational channel has enhanced wave energy at the shoreline. To assess the potential linkage between the deepened channel and incident wave energy flux at the shoreline in the realistic domain, model cases were run using modern bathymetry (2013/2014) and historical bathymetry prior to dredging (1848). In 1848 the natural depth of the channel in the upper estuary ranged from 5 to 7 m (Figure 13a), whereas the mean depth of the modern channel is currently 14 m. In the lower estuary, many of the longitudinal shoals are shallower in the modern bathymetry than in the historical conditions possibly owing to sediment resuspension driven by the near-bottom orbital velocities associated with locally intensified bottom friction. Correspondingly, wave heights in the lower bay are slightly lower (around 0.2 m) with the modern bathymetry due to attenuation by bottom friction over the longitudinal shoals. However, overall the difference in wave height between the modern and historical bathymetry is small, suggesting that deepening of the navigational channel has not significantly enhanced wave heights (Figure 13b). The results from the modern bathymetry (Figure 8f) show that for both up- and down-estuary wind forcing, the waves in the channel are always smaller than their equilibrium values, even for winds directed roughly along the channel direction. To explain the disequilibrium wave heights in the deep, narrow channel, the width-to-equilibrium-wave-height relationship (limited only by channel width) was calculated for comparison with waves propagating through a channel with different width. Model results using the idealized, uniform channel configuration suggest that wave height depends on channel width due to directional spreading. The shallower water on either side refracts the waves, directing wave energy out of the channel onto the shoals. The realistic domain shows the same influence of the narrow channel as the idealized case, with significantly lower wave heights than equilibrium in the channel, so the effect of the deepening is small on the overall wave energy budget for the estuary.

5. Conclusions

To understand complex interactions between the bathymetry and waves in estuaries and embayments, a coupled wave and circulation model was utilized in conjunction with field observations to evaluate the mechanisms that controlling wave energy in an estuary with spatially heterogenous bathymetry. Modeled water surface elevation and significant wave heights were calibrated with observed water level and waves during calm and energetic wind conditions at multiple locations including the navigational channel, on the channel flanks, and near the edge of tidal marsh. The model results show that waves in the lower bay depend on both local wind forcing and remote wave forcing from offshore, but waves in the rest of the estuary are controlled only by the local winds and the response of the wavefield to bathymetric variability. The numerical simulations also show that, under typical northerly wind conditions, waves are fetch-limited in the middle estuary and at equilibrium with local water depth only in the downwind region. During southerly wind conditions typical of storms, wave energy is near equilibrium in the lower bay, and midestuary waves are attenuated by the combination of whitecapping and bottom friction over the steep, longitudinal shoals. Wave energy dissipation is strongly tied to spatial gradients in bathymetry, particularly in the lower bay, as waves that are at equilibrium in deeper water propagated into shallower regions and are subject to greater bottom friction. These regions of enhanced frictional dissipation correspond with wave-induced bottom stresses that are more intensified locally than previously found in shallower and more spatially uniform estuaries (Karimpour et al., 2016, 2017; Mariotti et al., 2010; Mariotti & Fagherazzi, 2013). Although the energy dissipation due to bottom friction is small overall compared with dissipation by whitecapping, over steeply sloping topography bottom friction dissipation greatly exceeds the equilibrium balance. Wave heights exceed the local equilibrium depth in the downwind region, as the rate of wave growth due to more pronounced shoaling effect in this region exceeds wave dissipation rates leading to a convergence of wave energy. However, directional spreading as waves propagate along the channel cause a divergence in wave energy toward the shoals, reducing the wave height in the channel so wave heights do not equilibrate with the full channel depth.

The modeled incident wave energy flux at the shoreline has similar spatial distribution as the observed rates of shoreline retreat averaged over the past hundred years. On both the Delaware and New Jersey coasts, regions with some of the most severe shoreline retreat correspond with locally intensified wave energy

flux. Under representative wind conditions, the variations of incident wave energy flux at the shoreline correspond roughly to variations of historical shoreline retreat, with rapid rates of retreat in regions with intense wave energy and less change in regions that are shadowed by longitudinal shoals. Comparison between model cases using historical bathymetry prior to major dredging operations and modern conditions indicates little change in the wave climate associated with the presence of the navigational channel. Waves in the deep but narrow channel are always less than equilibrium height for the channel depth due to directional spread of the wave energy, so despite the large increase in channel depth, the changes in wave amplitude in the adjacent shallow subtidal and at the shoreline are minimal.

Acknowledgments
Funding was provided by National Science Foundation Coastal SEES: Toward Sustainable Urban Estuaries in the Anthropocene (OCE 1325136) and Ministry of Science and Technology (MOST 107-2611-M-006-004). We thank James Kirby, Fengyan Shi, and the two anonymous reviewers for their careful reading of our manuscript and their insightful comments. We thank Tracy Quirk for providing wave measurements in Bombay Hook, DE and Stow Creek, NJ. We thank Katie Pijanowski for compiling historical and modern bathymetric data for the estuary. Data supporting this study are posted to Zenodo (http://doi.org/10.5281/zenodo.1433055).

References

Abbot, M. B., & Price, W. A. (1994). *Coastal, estuarial, and harbor engineers' reference book* (1st ed.). London and New York: E & FN Spon. ISBN 0419154302

Battjes, J. A., & Stive, M. J. F. (1985). Calibration and verification of a dissipation model for random breaking waves. *Journal of Geophysical Research*, *90*(C5), 9159–9167. https://doi.org/10.1029/JC090iC05p09159

Boak, E. H., & Turner, I. L. (2005). Shoreline definition and detection: A review. *Journal of Coastal Research*, *21*, 688–703.

Booij, N., Ris, R. C., & Holthuijsen, L. H. (1999). A third-generation wave model for coastal regions: 1. Model description and validation. *Journal of Geophysical Research*, *104*(C4), 7649–7666. https://doi.org/10.1029/98JC02622

Bottema, M., de Waal, J. P., & Regeling, H. J. (2003). Some applications of the Lake IJssel/Lake Sloten wave data set. In J. McKee Smith (Ed.), *Coastal engineering 2002* (pp. 413–425). New York: American Society of Civil Engineers.

Bouws, E., & Komen, G. (1983). On the balance between growth and dissipation in an extreme depth-limited wind-sea in the southern North Sea. *Journal of Physical Oceanography*, *13*(9), 1653–1658. https://doi.org/10.1175/1520-0485(1983)013<1653:OTBBGA>2.0.CO;2

Chassignet, E. P., Arango, H. G., Dietrich, D., Ezer, T., Ghil, M., Haidvogel, D. B., et al. (2000). DAMEE-NAB: The base experiments. *Dynamics of Atmospheres and Oceans*, *32*, 155–183.

Chernetsky, A. S., Schuttelaars, H. M., & Talke, S. A. (2010). The effect of tidal asymmetry and temporal settling lag on sediment trapping in tidal estuaries. *Ocean Dynamics*, *60*(5), 1219–1241. https://doi.org/10.1007/s10236-010-0329-8

Cox, R., Wadsworth, R. A., & Thomson, A. G. (2003). Long-term changes in salt marsh extent affected by channel deepening in a modified estuary. *Continental Shelf Research*, *23*(17-19), 1833–1846. https://doi.org/10.1016/j.csr.2003.08.002

Crowell, M., Leatherman, S. P., & Buckley, M. K. (1991). Historical shoreline change: Error analysis and mapping accuracy. *Journal of Coastal Research*, *7*, 839–852.

De Waal, J. P. (2002). Wave growth limit in shallow water. In B. L. Edge & J. Michael Hemsley (Eds.), *Ocean wave measurement and analysis* (pp. 580–589). Reston, VA: American Society of Civil Engineers.

DiLorenzo, J. L., Huang, P., Thatcher, M. L., & Najarian, T. O. (1993). Dredging impacts on Delaware estuary tides, 3rd International Conference, waterway, port, coastal ocean div./ASCE. In *Estuarine and coastal modelling III* (pp. 86–103). Illinois: Oak Brook.

Fletcher, C. H., Knebel, H. J., & Kraft, J. C. (1990). Holocene evolution of an estuarine coast and tidal wetlands. *Geological Society of America Bulletin*, *102*(3), 283–297.

French, G. T. (1990). Historical shoreline changes in response to environmental conditions in West Delaware Bay. M.S. Thesis, Department of geography, University of Maryland, College Park, MD. 240 pp.

Green, M. O., & Coco, G. (2007). Sediment transport on an estuarine intertidal flat: Measurements and conceptual model of waves, rainfall and exchanges with a tidal creek. *Estuarine, Coastal and Shelf Science*, *72*(4), 553–569. https://doi.org/10.1016/j.ecss.2006.11.006

Green, M. O., & Coco, G. (2014). Review of wave driven sediment resuspension and transport in estuaries. *Reviews of Geophysics*, *52*, 77–117. https://doi.org/10.1002/2013RG000437

Haidvogel, D. B., Arango, H. G., Hedstrom, K., Beckmann, A., Malanotte-Rizzoli, P., & Shchepetkin, A. F. (2000). Model evaluation experiments in the North Atlantic Basin: Simulations in nonlinear terrain-following coordinates. *Dynamics of Atmospheres and Oceans*, *32*, 239–281.

Hasselmann, K., Barnett, T. P., Bouws, E., Carlson, H., Cartwright, D. E., Enke, K., et al. (1973). Measurements of wind-wave growth and swell decay during the Joint North Sea Wave Project (JONSWAP). *Ergnzungsheft zur Deutschen Hydrographischen Zeitschrift Reihe*, *A(8)*, 12, 95.

Holthuijsen, L. H., Zijlema, M., & van der Ham, P. J. (2008). Wave physics in a tidal inlet. In J. McKee Smith (Ed.), *Coastal engineering* (pp. 437–448). New York: American Society of Civil Engineers.

Hwang, P. A. (2006). Duration and fetch-limited growth functions of wind-generated waves parameterized with three different scaling wind velocities. *Journal of Geophysical Research*, *111*, C02005. https://doi.org/10.1029/2005JC003180

Jonsson, I. G. (1980). A new approach to rough turbulent boundary layers. *Ocean Engineering*, *7*(1), 109–152. https://doi.org/10.1016/0029-8018(80)90034-7

Karimpour, A., Chen, Q., & Jadhav, R. (2013). Turbidity dynamics in upper Terrebonne Bay, Louisiana. In A. Khan & W. Wu (Eds.), *Sediment transport: Monitoring* (pp. 339–360). Nova Sc. Pub: Modeling and Management.

Karimpour, A., Chen, Q., & Twilley, R. R. (2016). A field study of how wind waves and currents may contribute to the deterioration of saltmarsh fringe. *Estuaries and Coasts*, *39*(4), 935–950. https://doi.org/10.1007/s12237-015-0047-z

Karimpour, A., Chen, Q., & Twilley, R. R. (2017). Wind wave behavior in fetch and depth limited estuaries. *Scientific Reports*, *7*(1), 40,654. https://doi.org/10.1038/srep40654

Kearney, M. S., Rogers, A. S., Townshend, J. R. G., Rizzo, E., Stutzer, D., Stevenson, J. C., & et al. (2002). Landsat imagery shows decline of coastal marshes in Chesapeake and Delaware Bays. *Eos*, *83*, 17–178.

Keen, T. R., Rogers, W. E., Dykes, J., Kaihatu, J. M., & Holland, K. T. (2007). Determining heterogeneous bottom friction distributions using a numerical wave model. *Journal of Geophysical Research*, *112*, C08008. https://doi.org/10.1029/2005JC003309

Komen, G. J., Hasselmann, S., & Hasselmann, K. (1984). On the existence of a fully developed wind-sea spectrum. *Journal of Physical Oceanography*, *14*(8), 1271–1285. https://doi.org/10.1175/1520-0485(1984)014<1271:OTEOAF>2.0.CO;2

Kraft, J. C., Yi, H., & Khalequzzaman, M. (1992). Geologic and human factors in the decline of the tidal salt marsh lithosome: The Delaware estuary and Atlantic coastal zone. *Sedimentary Geology*, *80*(3-4), 233–246. https://doi.org/10.1016/0037-0738(92)90043-Q

Kukulka, T., Jenkins, R. L., Kirby, J. T., Shi, F., & Scarborough, R. W. (2017). Surface wave dynamics in Delaware Bay and its adjacent coastal shelf. *Journal of Geophysical Research: Oceans*, *122*, 8683–8706. https://doi.org/10.1002/2017JC013370

Lin, W., Sanford, L. P., & Suttles, S. E. (2002). Wave measurement and modeling in Chesapeake Bay. *Continental Shelf Research*, *22*(18-19), 2673–2686. https://doi.org/10.1016/S0278-4343(02)00120-6

Liria, P., Garel, E., & Uriarte, A. (2009). The effects of dredging operations on the hydrodynamics of an ebb tidal: Oka Estuary, northern Spain. *Continental Shelf Research*, *29*(16), 1983–1994. https://doi.org/10.1016/j.csr.2009.01.014

Luettich, R. A., & Westerink, J. J. (1992). A solution for the vertical variation of stress, rather than velocity, in a three-dimensional circulation model. *International Journal for Numerical Methods in Fluids*, *12*(10), 911–928. https://doi.org/10.1002/fld.1650121002

Madsen, O. S., Poon, Y. K., & Graber, H. C. (1988). Spectral wave attenuation by bottom friction: Theory, Proc. 21st Int. Conf. coastal engineering, ASCE, 492–504.

Marani, M., D'Alpaos, A., Lanzoni, S., & Santalucia, M. (2011). Understanding and predicting wave erosion of marsh edges. *Geophysical Research Letters*, *38*, L21401. https://doi.org/10.1029/2011GL048995

Mariotti, G., & Fagherazzi, S. (2013). Wind waves on a mudflat: The influence of fetch and depth on bed shear stresses. *Continental Shelf Research*, *60*(Supplement), S99–S110. https://doi.org/10.1016/j.csr.2012.03.001

Mariotti, G., Fagherazzi, S., Wiberg, P. L., McGlathery, K. J., Carniello, L., & Defina, A. (2010). Influence of storm surges and sea level on shallow tidal basin erosive processes. *Journal of Geophysical Research*, *115*, C11012. https://doi.org/10.1029/2009JC005892

Massel, S. R. (1996). *Ocean surface waves: Their physics and predictions* (Vol. 11). London: Advanced Series on Coastal Engineering.

Maurmeyer, E. M. (1978). Geomorphology and evolution of transgressive estuarine washover barrier along the western shore of the Delaware Bay. Thesis, geology department, University of Delaware.

McLoughlin, S. M., Wiberg, P. L., Safak, I., & McGlathery, K. J. (2015). Rates and forcing of marsh edge erosion in a shallow Coastal Bay. *Estuaries and Coasts*, *38*(2), 620–638. https://doi.org/10.1007/s12237-014-9841-2

McSweeney, J. M., Chant, R. J., & Sommerfield, C. K. (2016). Lateral variability of sediment transport in the Delaware Estuary. *Journal of Geophysical Research: Oceans*, *121*, 725–744. https://doi.org/10.1002/2015JC010974

Murphy, A. H. (1988). Skill scores based on the mean square error and their relationships to the correlation coefficient. *Monthly Weather Review*, *116*(12), 2417–2424. https://doi.org/10.1175/1520-0493(1988)116<2417:SSBOTM>2.0.CO;2

National Oceanographic and Atmospheric Administration (2014). National Ocean Service Hydrographic Survey data. Retrieved from https://www.ngdc.noaa.gov/mgg/bathymetry/hydro.html

Nikuradse, J. (1933). Laws of flow in rough pipes. VDI Forschungsheft 361. In Translation, National Advisory Committee for Aeronautics Technical Memorandum 1292, 1950.

Padilla-Hernández, R., & Monbaliu, J. (2001). Energy balance of wind waves as a function of the bottom friction formulation. *Coastal Engineering*, *43*(2), 131–148. https://doi.org/10.1016/S0378-3839(01)00010-2

Phillips, J. D. (1986). Spatial analysis of shoreline erosion, Delaware Bay, New Jersey. *Annals of the Association of American Geographers*, *76*(1), 50–62. https://doi.org/10.1111/j.1467-8306.1986.tb00103.x

Pierson, W. J., & Moskowitz, L. (1964). A proposed spectral form for fully developed wind seas based on the similarity theory of S. A. Kitaigorodskii. *Journal of Geophysical Research*, *69*(24), 5181–5190. https://doi.org/10.1029/JZ069i024p05181

Pijanowski, K. (2016). Patterns and rates of historical shoreline change in the Delaware Estuary, master thesis, University of Delaware. http://gradworks.umi.com/10/19/10191317.html

Ralston, D. K., Cowles, G. W., Geyer, W. R., & Holleman, R. C. (2016). Turbulent and numerical mixing in a salt wedge estuary: Dependence on grid resolution, bottom roughness, and turbulence closure. *Journal of Geophysical Research: Oceans*, *122*, 692–712. https://doi.org/10.1002/2016JC011738

Sanford, L. P., & Gao, J. (2018). Influences of wave climate and sea level on shoreline erosion rates in the Maryland Chesapeake Bay. *Estuaries and Coasts*, *41*(Suppl 1), 19–37. https://doi.org/10.1007/s12237-017-0257-7

Schwimmer, R. A. (2001). Rates and processes of marsh shoreline erosion in Rehoboth Bay, Delaware, U.S.A. *Journal of Coastal Research*, *17*(3), 672–683.

Talke, S. A., de Swart, H. E., & de Jonge, V. N. (2009). An idealized model and systematic process study of oxygen depletion in highly turbid estuaries. *Estuaries and Coasts* https://doi.org/10.1007/s12237-009-9171-y, *32*(4), 602–620.

Thieler, E. R., Himmelstoss, E. A., Zichichi, J. L., & Ergul, A. (2009). Digital Shoreline Analysis System (DSAS) version 4.0—An ArcGIS extension for calculating shoreline change: U.S. Geological Survey open-file report 2008 1278.*current version 4.3, 79.

United States Army Corps of Engineers (2014). Philadelphia to Sea Bathymetric Survey Data. Retrieved from http://www.nap.usace.army.mil/Missions/Civil-Works/Surveys/Projects/

van der Westhuysen, A. J. (2010). Modeling of depth-induced wave breaking under finite depth wave growth conditions. *Journal of Geophysical Research*, *115*, C01008. https://doi.org/10.1029/2009JC005433

van der Westhuysen, A. J., Zijlema, M., & Battjes, J. A. (2007). Nonlinear saturation-based whitecapping dissipation in SWAN for deep and shallow water. *Coastal Engineering*, *54*(2), 151–170. https://doi.org/10.1016/j.coastaleng.2006.08.006

Warner, J. C., Sherwood, C. R., Arango, H. G., & Signell, R. P. (2005). Performance of four turbulence closure models implemented using a generic length scale method. *Ocean Modelling*, *8*, 81–113.

Warner, J. C., Armstrong, B., He, R., & Zambon, J. B. (2010). Development of a coupled ocean-atmosphere-wave-sediment transport (coawst) modeling system. *Ocean Modelling*, *35*(3), 230–244. https://doi.org/10.1016/j.ocemod.2010.07.010

Weber, S. L. (1991a). Bottom friction for wind sea and swell in extreme depth-limited situations. *Journal of Physical Oceanography*, *21*(1), 149–172. https://doi.org/10.1175/1520-0485(1991)021<0149:BFFWSA>2.0.CO;2

Weber, S. L. (1991b). Eddy-viscosity and drag-law models for random ocean wave dissipation. *Journal of Fluid Mechanics*, *232*(1), 73–98. https://doi.org/10.1017/S0022112091003634

Young, I. R., & Babanin, A. V. (2006). The form of the asymptotic depth-limited wind wave frequency spectrum. *Journal of Geophysical Research*, *111*, C06031. https://doi.org/10.1029/2005JC003398

Young, I. R., & Verhagen, L. A. (1996a). The growth of fetch limited waves in water of finite depth. Part I: Total energy and peak frequency. *Coastal Engineering*, *28*, 47–78.

Young, I. R., & Verhagen, L. A. (1996b). The growth of fetch limited waves in water of finite depth. Part II: Spectral evolution. *Coastal Engineering*, *28*, 79–100.

Zakharov, V. E. (2005). Theoretical interpretation of fetch limited wind-driven sea observations. *Nonlinear Processes in Geophysics*, *12*(6), 1011–1020. https://doi.org/10.5194/npg-12-1011-2005